



UNIVERSITY OF LEEDS

This is a repository copy of *Two-dimensional Sc<sub>2</sub>N MXenes as efficient solid catalysts for CO<sub>2</sub> adsorption and conversion: a density functional theory study*.

White Rose Research Online URL for this paper:

<https://eprints.whiterose.ac.uk/id/eprint/230488/>

Version: Accepted Version

---

**Article:**

Parto, M., Tafreshi, S.S. and De Leeuw, N. orcid.org/0000-0002-8271-0545 (Accepted: 2025) Two-dimensional Sc<sub>2</sub>N MXenes as efficient solid catalysts for CO<sub>2</sub> adsorption and conversion: a density functional theory study. Philosophical Transactions of the Royal Society A: Mathematical, Physical and Engineering Sciences. ISSN: 1364-503X (In Press)

---

This is an author produced version of an article accepted for publication in Philosophical Transactions of the Royal Society A: Mathematical, Physical and Engineering Sciences made available under the terms of the Creative Commons Attribution License (CC-BY), which permits unrestricted use, distribution and reproduction in any medium, provided the original work is properly cited.

**Reuse**

This article is distributed under the terms of the Creative Commons Attribution (CC BY) licence. This licence allows you to distribute, remix, tweak, and build upon the work, even commercially, as long as you credit the authors for the original work. More information and the full terms of the licence here: <https://creativecommons.org/licenses/>

**Takedown**

If you consider content in White Rose Research Online to be in breach of UK law, please notify us by emailing [eprints@whiterose.ac.uk](mailto:eprints@whiterose.ac.uk) including the URL of the record and the reason for the withdrawal request.



[eprints@whiterose.ac.uk](mailto:eprints@whiterose.ac.uk)  
<https://eprints.whiterose.ac.uk/>

# Two-dimensional Sc<sub>2</sub>N MXenes as efficient solid catalysts for CO<sub>2</sub> adsorption and conversion: a density functional theory study

Masoumeh Parto<sup>1</sup>, Saeedeh Sarabadani Tafreshi<sup>1,2,\*</sup>, Nora H. de Leeuw<sup>2,3\*</sup>

<sup>1</sup>Department of Chemistry, Amirkabir University of Technology, No.350, Hafez Avenue, Valiasr Square, 1591634311 Tehran, Iran

<sup>2</sup>School of Chemistry, University of Leeds, LS2 9JT Leeds, UK

<sup>3</sup>Department of Earth Sciences, Utrecht University, 3584 CB Utrecht, The Netherlands

\*Corresponding authors: [s.s.tafreshi@aut.ac.ir](mailto:s.s.tafreshi@aut.ac.ir); [n.h.deleeuw@leeds.ac.uk](mailto:n.h.deleeuw@leeds.ac.uk)

## Abstract

We have employed density functional theory (DFT) calculations to explore the catalytic potential of scandium nitride (Sc<sub>2</sub>N) MXenes for CO<sub>2</sub> capture and hydrogenation to methane. The Sc<sub>2</sub>N surface exhibits a strong affinity for CO<sub>2</sub> with an adsorption energy of  $-3.627$  eV, surpassing values reported for other MXenes such as Ti<sub>2</sub>N and V<sub>2</sub>N, and even outperforming conventional catalysts like Pt(111). Charge density difference and COHP analyses reveal significant back-donation from Sc d-orbitals to the antibonding orbitals of CO<sub>2</sub>, resulting in the formation of activated CO<sub>2</sub><sup>δ-</sup> species. AIMD simulations confirm the thermal stability of Sc<sub>2</sub>N under ambient conditions. The hydrogenation pathway to CH<sub>4</sub> proceeds via eight elementary steps, with the CH<sub>2</sub>OH + H → CH<sub>3</sub>OH reaction identified as the rate-determining step due to its high activation barrier (2.916 eV). Sc<sub>2</sub>N effectively stabilizes key intermediates such as COOH, HCOOH, and CH<sub>2</sub>OH, and facilitates H<sub>2</sub> dissociation with moderate energy requirements. Compared to other MXenes, Sc<sub>2</sub>N shows superior ability to stabilize intermediates, particularly HCOOH, which plays a crucial role in the conversion pathway. However, large negative adsorption energies for H and O atoms suggest potential surface poisoning, which may limit catalytic turnover unless regeneration strategies are implemented. These findings highlight Sc<sub>2</sub>N MXenes as robust and efficient materials for CO<sub>2</sub> capture and conversion, although further optimization is necessary for sustained catalytic performance.

**Key Words:** MXenes, Catalysis, Density Functional Theory, CO<sub>2</sub> Hydrogenation

## 1. Introduction

Since the onset of the second industrial revolution,<sup>1</sup> characterized by increasing automation and mass production, the global production of various entities, e.g. cement, electricity, energy, and goods for household consumption, has relied heavily on the combustion of fossil fuels<sup>2</sup>. However, this practice has resulted in the substantial release of carbon dioxide (CO<sub>2</sub>) into the Earth's atmosphere<sup>3</sup>, with global carbon dioxide emissions surging by more than 70% between 1970 and 2002<sup>4</sup>. Unfortunately, this anthropologic production of CO<sub>2</sub> is no longer balanced by natural capture, conversion and storage. CO<sub>2</sub> is a potent greenhouse gas<sup>5</sup> that contributes to the rise in the Earth's temperature through the trapping and re-emission of infrared radiation<sup>6, 7</sup>. The consequences of global warming are far-reaching and include phenomena such as floods, droughts, and the extinction of plant and animal species<sup>8</sup>. In view of this harmful climate change, the capture and transformation of CO<sub>2</sub> into benign or even beneficial products has become paramount.

Carbon dioxide is a linear and remarkably stable molecule, featuring carbon in its highest oxidation state, and the C=O bond within CO<sub>2</sub> is thermodynamically stable<sup>9</sup>. Disrupting this bond and activating carbon dioxide for further reactions requires a substantial amount of energy and high temperatures<sup>9</sup>. Furthermore, the chemical stability of carbon dioxide underscores its weak interaction with solid surfaces. Effective CO<sub>2</sub> adsorption typically occurs at elevated temperatures and under significant partial pressures, often involving charge transfer processes that result in the creation of bent, anionic CO<sub>2</sub> species (CO<sub>2</sub><sup>δ-</sup>)<sup>10</sup>. The use of solid catalysts has garnered significant attention in this process, owing to their non-corrosive nature, cost-effectiveness, and ease of regeneration, making them advantageous for CO<sub>2</sub> capture and conversion<sup>11, 12</sup>, which is the basis for many of the approaches suggested for carbon capture and utilisation (CCU) strategies to mitigate CO<sub>2</sub> emissions<sup>13</sup>.

Recent years have witnessed the development of two-dimensional materials with exceptional properties, including extraordinarily high specific surface areas with substantial proportions of exposed surface atoms, rendering them promising candidates for CO<sub>2</sub> adsorption and reduction. Among these materials, MXenes have emerged as a notable group. MXenes are derived from transition metal carbides and nitrides and are obtained from MAX phases with the formula M<sub>n+1</sub>AX<sub>n</sub>, where M represents the transition metal, A is an element from group 13 or 14 of the periodic table, X is either carbon or nitrogen, and the value of n, which ranges from 1 to 3, determines the atomic layers of the resulting material, ranging from 3 or 5 to 7 layers<sup>14</sup>. The two-

dimensional structure of MXenes, facilitated by the presence of vacant d orbitals of the metals in their surfaces, enables efficient gas adsorption<sup>15</sup>. In a groundbreaking development in 2011, MXenes were first synthesized through the production of  $\text{Ti}_3\text{C}_2$  during an etching process, accomplished by dissolving  $\text{Ti}_3\text{AlC}_2$  in hydrofluoric acid<sup>16</sup>. Most MXenes are synthesized through a three-layer hexagonal etching process of the MAX phase using various acids, effectively removing layer A from the structure and yielding two-dimensional MXenes<sup>17, 18</sup>. For example,  $\text{Sc}_2\text{N}$  MXene can be produced from the  $\text{Sc}_2\text{AlN}$  MAX phase by removing the aluminum (Al) layer through chemical etching, using acids like hydrofluoric acid (HF), or through molten salt processes<sup>19, 20</sup>. After etching, the resulting two-dimensional structure consists of a hexagonal arrangement of scandium and nitrogen atoms, with exposed active sites that can interact with gas molecules such as  $\text{CO}_2$ .

Notably, the substantial adsorption energy released by carbon dioxide binding to  $\text{M}_2\text{N}$  surfaces compared to similar carbides ( $\text{M}_2\text{C}$ ) positions  $\text{M}_2\text{N}$  materials as the more suitable candidates for  $\text{CO}_2$  activation and conversion, which show enhanced  $\text{CO}_2$  adsorption and catalytic properties owing to their electron-rich nitrogen layers<sup>10</sup>.

Recent efforts have focused on tailoring MXene surfaces through functionalization or heterostructure design to improve catalytic selectivity and reduce energy barriers for  $\text{CO}_2$  hydrogenation<sup>21</sup>. Moreover, very recent studies have demonstrated that tuning the electronic properties of MXene materials via compositional engineering or metal-support interactions can yield promising results in terms of both adsorption capacity and catalytic turnover for  $\text{CO}_2$  reduction to  $\text{CH}_4$  and other value-added products<sup>22, 23</sup>.

Scandium nitride ( $\text{Sc}_2\text{N}$ ) MXenes, in particular, present a promising material for catalytic applications. First-principles calculations have predicted the thermodynamic stability, structural robustness, and metallic conductivity of Sc-based MXenes, highlighting their potential as a promising 2D catalyst<sup>24</sup>. Further studies have examined the influence of surface terminations, magnetism, and charge transport in Sc-based MXenes<sup>19, 25</sup>. The unique structural features of MXenes, including their tuneable surface chemistry and electronic properties, have been studied extensively by researchers, who have highlighted the role of surface terminations (e.g., -O, -OH, and -F groups) in modulating the adsorption properties of MXenes. Such surface modifications can further enhance the catalytic performance of  $\text{Sc}_2\text{N}$  by tailoring its electronic structure to facilitate  $\text{CO}_2$  reduction<sup>26</sup>. Recent work also points to the high carrier mobility and low work

function of  $\text{Sc}_2\text{N}$ , which are favourable for electronic and catalytic applications<sup>24, 26</sup>. In addition, related scandium-based MXenes such as  $\text{Sc}_2\text{C}$  have been investigated for thermoelectric applications, where surface functionalization was shown to enhance the Seebeck coefficient and improve overall energy conversion performance<sup>27</sup>. Furthermore, doped Sc-based MXenes have recently been predicted to exhibit s–p–d band inversion, identifying them as a new class of topological insulator with potential relevance for quantum and spintronic devices.<sup>28</sup> Recent experimental work has demonstrated that two-dimensional functionalized Sc-based MXenes synthesized via sputtering exhibit semiconductive behaviour with strong optical absorption in the visible region, suggesting their potential for optoelectronic and photocatalytic applications.<sup>29</sup> Moreover,  $\text{Sc}_2\text{N}$  has been highlighted in computational screening studies of MXenes for  $\text{H}_2$  adsorption and dissociation, where its electron-rich nitrogen layers promote strong binding with molecules<sup>30</sup>. Although there have only been limited studies on  $\text{Sc}_2\text{N}$ , theoretical research indicates that it exhibits stronger  $\text{CO}_2$  adsorption energies compared to other MXenes, e.g.  $\text{Ti}_2\text{N}$  and  $\text{Zr}_2\text{N}$ <sup>31</sup>.

In this context, our study employs calculations based on the density functional theory (DFT) to investigate the  $\text{CO}_2$  adsorption and hydrogenation behaviour on  $\text{Sc}_2\text{N}$  monolayers, evaluating its capacity to catalytically convert  $\text{CO}_2$  to methane. The findings are discussed in relation to prior theoretical insights into  $\text{Sc}_2\text{N}$  and broader MXene-based  $\text{CO}_2$  reduction mechanisms.

## 2. Computational Models and Methods

In this work, we have constructed the monolayer structure of  $\text{Sc}_2\text{N}$  MXene based on crystallographic data, before performing full geometry optimization using density functional theory calculations. The optimized structure is shown in Figure 1 and consists of a hexagonal arrangement of scandium and nitrogen atoms in a layered configuration. A triclinic unit cell with lattice constants of  $a = 12.685 \text{ \AA}$ ,  $b = 12.685 \text{ \AA}$ , and  $c = 14.408 \text{ \AA}$  was optimized to achieve a stable surface configuration. The sandwich-like arrangement of scandium atoms on both sides of the nitrogen layer offers enhanced surface reactivity, similar to what has been observed in  $\text{Ti}_2\text{N}$  and  $\text{Nb}_2\text{N}$  MXenes<sup>25</sup>.

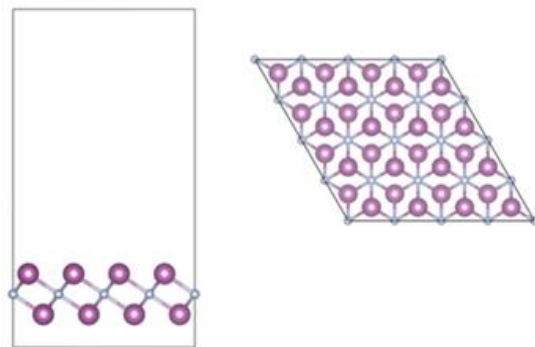


Figure 1. Side and top views of the optimized  $\text{Sc}_2\text{N}$  MXene structure used in the DFT calculations (Sc = purple, N = blue). The structure features a layered hexagonal configuration with exposed scandium atoms in both surfaces.

The electronic structures and catalytic properties of  $\text{Sc}_2\text{N}$  MXenes were investigated via density functional theory (DFT)<sup>32,33</sup> calculations using the Vienna Ab initio Simulation Package (VASP)<sup>34-36</sup>. The generalized gradient approximation (GGA)<sup>37</sup> was applied with the Perdew-Burke-Ernzerhof (PBE) functional<sup>38</sup>, which has been used widely in studies of  $\text{CO}_2$  adsorption at various MXenes<sup>39</sup>. The interaction between the valence electron density and the core electrons is described using the projector augmented wave (PAW) method<sup>40</sup>. Similar computational frameworks have been employed in other studies on  $\text{CO}_2$  adsorption at metal oxides and MOFs, where DFT simulations have provided critical insights into interaction mechanisms at the atomic level<sup>41,42</sup>.

A plane-wave cut-off energy of 800 eV was used, which was determined through convergence tests, as shown in Figure 1S-a, in the Electronic Supporting Information (ESI). The choice of this energy cut-off is critical to ensure the convergence of the results. Previous research on  $\text{Ti}_3\text{C}_2$  and  $\text{Nb}_2\text{N}$  MXenes has demonstrated that cut-off energies in the range of 500–800 eV are sufficient to ensure accurate simulation results at an acceptable computational cost<sup>43</sup>. Monkhorst-Pack k-point grids of  $5 \times 5 \times 1$  and  $11 \times 11 \times 1$  were employed to sample the Brillouin zone, ensuring high precision in the calculation of adsorption energies and electronic interactions<sup>44</sup>, respectively, as illustrated in Figure 1S-b in the ESI.

Long-range dispersion interactions were accounted for using the Grimme D3 correction scheme, which was included in all calculations to improve the accuracy of adsorption energies and weak intermolecular interactions, consistent with previous studies on catalytic systems.<sup>45-47</sup>

The  $\text{CO}_2$  adsorption process on the  $\text{Sc}_2\text{N}$  surface was modelled by placing a  $\text{CO}_2$  molecule at various potential adsorption sites, including the top, bridge, and hollow sites. The adsorption energy for each molecule at the surface was then calculated using the following formula:

$$E_{ads} = E_{A+slab} - E_{slab} - E_A \quad (1)$$

In this equation,  $E_{ads}$  represents the adsorption energy,  $E_{A+slab}$  corresponds to the energy of the system of an adsorbed molecule on the catalyst surface, and  $E_A$  and  $E_{slab}$  denote the energies of the isolated molecule in a vacuum and the energy of the pristine surface, respectively. A large negative  $E_{ads}$  value indicates a stable configuration and exothermic adsorption.<sup>48</sup>

To simulate the hydrogenation of each adsorbed  $\text{CO}_2$ ,  $\text{COOH}$ ,  $\text{HCOOH}$ ,  $\text{HCO}$ ,  $\text{H}_2\text{CO}$ ,  $\text{CH}_2\text{OH}$ ,  $\text{CH}_3\text{OH}$ , and  $\text{CH}_3$  molecule, a hydrogen atom must be positioned appropriately according to the expected product of the hydrogenation reaction. In this regard, nine reactions were investigated from a selected pathway, comprising molecules and hydrogen gas as the initial state and progressing to the respective products. The reaction energy for each step was calculated using the following equation:

$$E_{reac} = E_f - E_{in} \quad (2)$$

where  $E_f$  represents the energy of the final state and  $E_{in}$  represents the energy of the initial state.

The Nudged Elastic Band (NEB)<sup>49, 50</sup> method was employed to determine the reaction path and transition state between the reactant and product states. Intermediate states are identified, and the activation energy for each reaction is calculated using the following equation:

$$E_a = E_{TS} - E_{in} \quad (3)$$

where  $E_a$  represents the activation energy,  $E_{TS}$  is the energy of the intermediate state of the reaction, and  $E_{in}$  is the energy of the initial state in each reaction.

To assess the thermodynamic stability of the  $\text{Sc}_2\text{N}$  catalyst, we performed ab initio molecular dynamics (AIMD) simulations using the Nosé–Hoover thermostat in the NVT ensemble at 300 K for 20 ps with a time step of 1 fs as implemented in VASP package. The structural integrity of the  $\text{Sc}_2\text{N}$  surface was monitored throughout the trajectory, and the temperature and energy fluctuations were analyzed to confirm stability.

### 3. Results and Discussion

The optimized structure of the Sc<sub>2</sub>N MXene revealed a highly stable configuration, with minimal distortion during surface relaxation. This stability is essential in maintaining catalytic activity during reaction cycles, as structural degradation can lead to deactivation of the catalyst<sup>51</sup>. Similar surface stability has been observed in other MXenes, e.g. Ti<sub>2</sub>N and Zr<sub>2</sub>N<sup>52</sup>. To demonstrate the thermal stability of the catalyst, ab initio molecular dynamics (AIMD) simulations were performed for the Sc<sub>2</sub>N monolayer at 300 K. The results reveal that the structure remains stable over the entire 20 ps simulation, with no evidence of bond breaking, surface reconstruction, or significant distortion. As illustrated in Figure 3, the total energy fluctuates within a narrow range, while the system temperature remains consistently close to the target value, indicating effective thermal regulation by the Nosé–Hoover thermostat. Representative snapshots of the initial and final configurations (Figure 2) confirm the preservation of the surface morphology. These findings provide strong evidence of the thermodynamic robustness of Sc<sub>2</sub>N under ambient conditions, underscoring its suitability for practical catalytic applications.

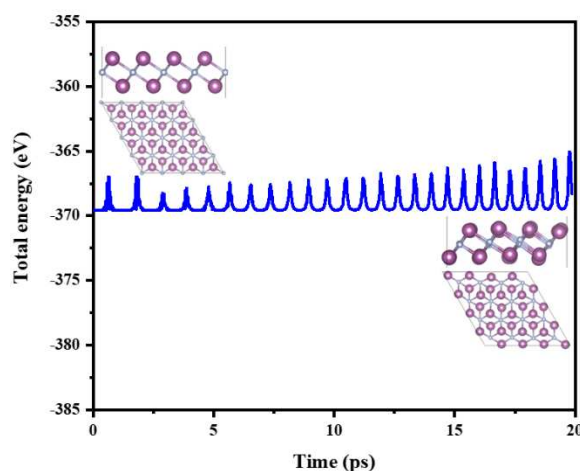
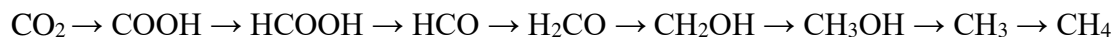


Figure 2. Time evolution of (a) total energy of the Sc<sub>2</sub>N surface during a 20 ps AIMD simulation at 300 K. Snapshots of the Sc<sub>2</sub>N surface at the start and end of the 20 ps AIMD simulation at 300 K were added.

The CO<sub>2</sub> reduction process focused on in this work involves eight elementary steps<sup>53</sup>, which can be represented as a pathway starting from CO<sub>2</sub> and proceeding through seven surface-bound intermediates as follows:





The intermediates were simulated and adsorbed at the Sc<sub>2</sub>N surface in different positions, with the optimal position for each molecule determined through geometry optimizations.

### 3.1. Sc<sub>2</sub>N Electronic Properties

The electronic structure of the Sc<sub>2</sub>N monolayer was elucidated through projected density of states (PDOS) analysis, as shown in Figure 3. The total density of states (TDOS) exhibits a prominent peak at the Fermi level (set to 0 eV), which clearly indicates the metallic nature of Sc<sub>2</sub>N. The absence of a band gap further supports its intrinsic metallicity, consistent with prior predictions for early transition metal-based MXenes<sup>24</sup>. The PDOS reveals that the states near the Fermi level are primarily derived from the Sc 3d-orbitals, while N 2p-orbitals mainly contribute to deeper valence states in the range of -6 to -3 eV. This orbital distribution suggests significant Sc–N hybridization, contributing to the structural stability and electronic delocalization. Moreover, the strong presence of unoccupied Sc d-states above the Fermi level implies high electronic activity, which can be beneficial for catalytic applications, such as hydrogen evolution or CO<sub>2</sub> reduction reactions. Similar behaviour has been reported in Ti<sub>2</sub>N and V<sub>2</sub>C MXenes, where conduction bands dominated by d-orbitals promote metallic conductivity and enhance surface reactivity<sup>16</sup>.

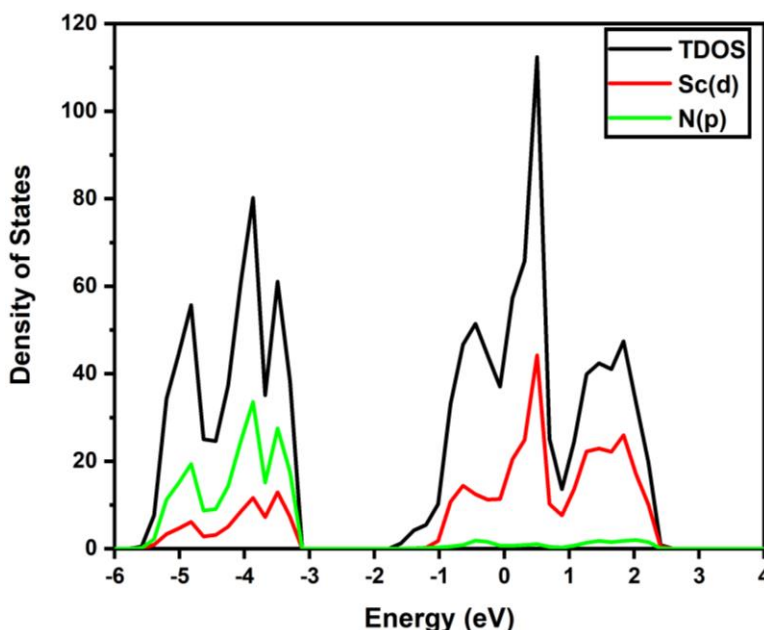


Figure 3. Orbital-projected density of states (PDOS) for the Sc<sub>2</sub>N monolayer. The total density of states (TDOS) is shown in black, while the contributions from Sc 3d and N 2p orbitals are shown in red and green, respectively. The Fermi level is set to 0 eV.

### 3.2. CO<sub>2</sub> Adsorption

One of the primary challenges in developing a heterogeneous catalyst for CO<sub>2</sub> adsorption, activation and reduction is establishing a robust interaction between CO<sub>2</sub> and the solid surface. The adsorption of CO<sub>2</sub> on the Sc<sub>2</sub>N surface was found to be highly favourable, with an adsorption energy of -3.627 eV. This interaction is stronger than those reported for other MXenes, such as Ti<sub>2</sub>N (-3.13 eV) and V<sub>2</sub>N (-1.67 eV)<sup>31</sup>. The hollow site, where both oxygen atoms of the CO<sub>2</sub> molecule can interact with scandium atoms, was determined to be the most stable adsorption configuration, as depicted in Figure 4, which is consistent with findings from previous studies on CO<sub>2</sub> adsorption at transition metal carbides and nitrides, where hollow sites often provide the most favourable binding energies<sup>54</sup>. In comparison, platinum-based catalysts, which are commonly used for CO<sub>2</sub> electro-reduction, do not adsorb CO<sub>2</sub> (adsorption energy of +0.51 eV), highlighting the superior CO<sub>2</sub> binding capacity of Sc<sub>2</sub>N<sup>55</sup>. The strong interaction between CO<sub>2</sub> and the Sc<sub>2</sub>N surface can be attributed to the electron-donating capability of the scandium d-orbitals, which facilitate back-donation to the CO<sub>2</sub> molecule, thereby enhancing adsorption and activating the CO<sub>2</sub> molecule ready for reduction<sup>31, 56, 57</sup>. To quantify this interaction, we have performed a Bader charge analysis<sup>58</sup>, which reveals a charge transfer of 1.746e<sup>-</sup> from the Sc<sub>2</sub>N surface to the CO<sub>2</sub> molecule. This substantial electron transfer suggests the formation of a CO<sub>2</sub><sup>δ-</sup> species, a key indicator of activation. Furthermore, the charge density difference plot shown in Figure 5 highlights charge accumulation around the CO<sub>2</sub> oxygen atoms and corresponding depletion around scandium atoms, consistent with d-orbital-mediated back-donation and confirming strong electronic coupling between the surface and the adsorbate. The charge density difference was calculated as  $\Delta\rho = \rho(\text{CO}_2/\text{Sc}_2\text{N}) - \rho(\text{Sc}_2\text{N}) - \rho(\text{CO}_2)$ , where  $\rho(\text{CO}_2/\text{Sc}_2\text{N})$  is the charge density of the adsorbed system,  $\rho(\text{Sc}_2\text{N})$  is the charge density of the clean surface, and  $\rho(\text{CO}_2)$  is the charge density of the isolated CO<sub>2</sub> molecule in the same configuration.

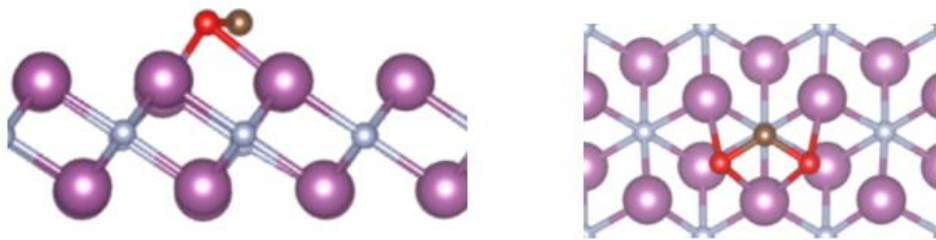


Figure 4. Side and top views of the adsorbed CO<sub>2</sub> molecule in the hollow position of the Sc<sub>2</sub>N surface (Sc = purple, N = blue, O = red, C = brown).

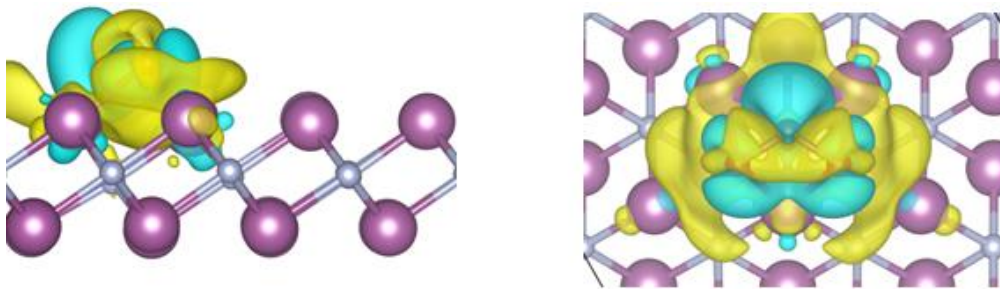


Figure 5. Side and top views of charge density difference plot for CO<sub>2</sub> adsorption on the Sc<sub>2</sub>N surface. Yellow and blue isosurfaces represent regions of charge depletion and accumulation, respectively (isosurface value =  $\pm 0.002$  e<sup>-</sup>/Å<sup>3</sup>).

To further explore the nature of the CO<sub>2</sub>–Sc<sub>2</sub>N interaction, we have also performed orbital-projected density of states (PDOS) analysis (Figure 6). The PDOS reveals pronounced overlap between the O 2p orbitals of CO<sub>2</sub> and the Sc 3d orbitals of the substrate around the Fermi level. This interaction is indicative of orbital hybridization and supports the presence of electron back-donation from Sc<sub>2</sub>N to the antibonding orbitals of CO<sub>2</sub>, facilitating its activation. These results are consistent with previous studies on MXene–CO<sub>2</sub> systems, where similar orbital interactions have been linked to strong chemisorption and efficient charge transfer<sup>59, 60</sup>.

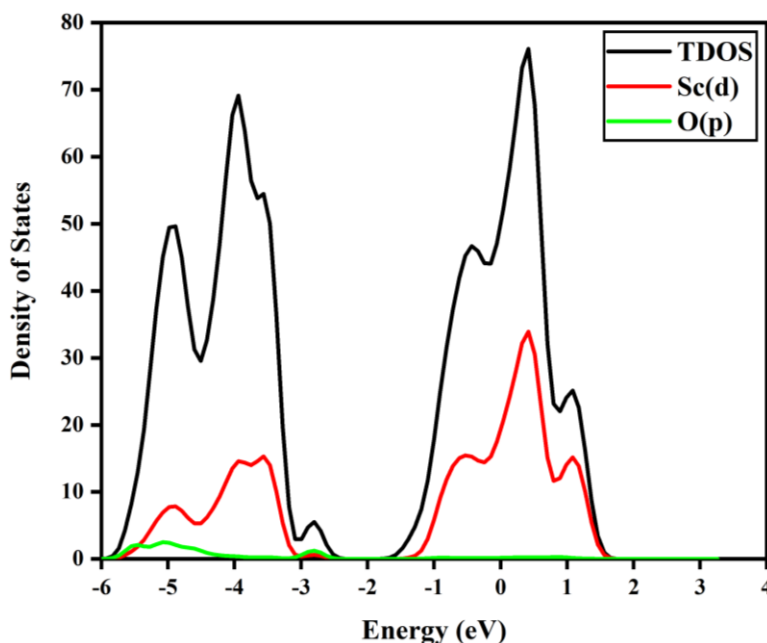
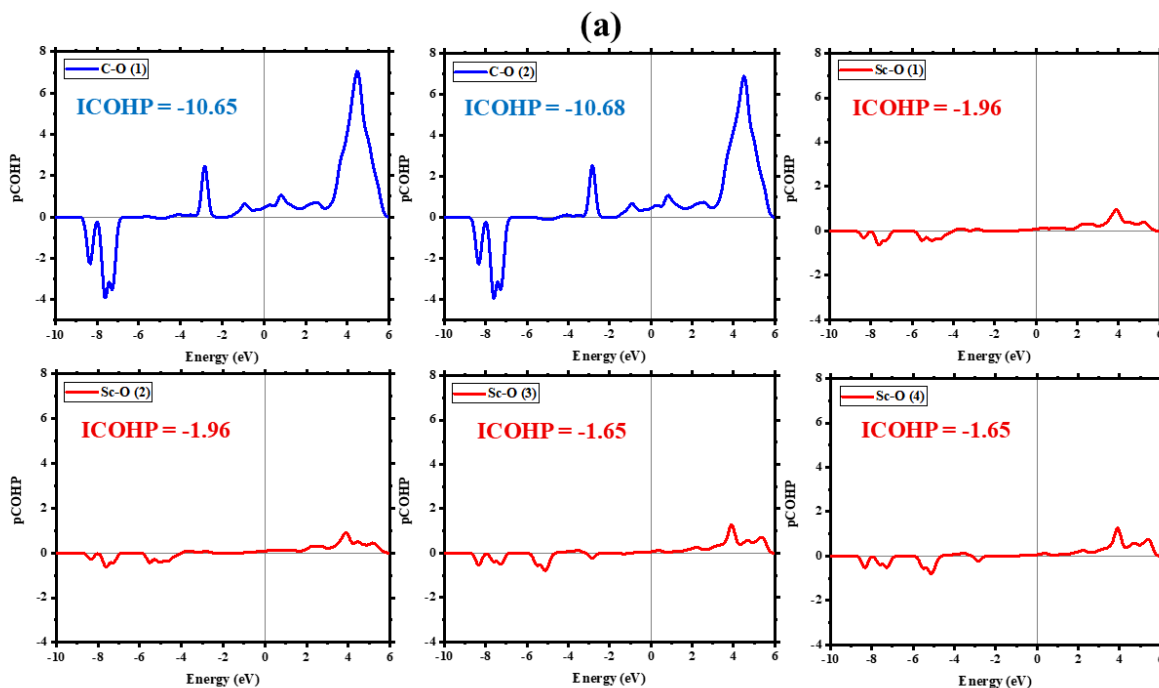


Figure 6. Orbital-projected density of states (PDOS) for the CO<sub>2</sub>–Sc<sub>2</sub>N system. The total density of states (TDOS) is shown in black, while the contributions from Sc 3d orbitals of Sc<sub>2</sub>N and O 2p orbitals of CO<sub>2</sub> are shown in red and green, respectively. The Fermi level is set to 0 eV.

To further investigate the bonding nature and interaction mechanism between CO<sub>2</sub> and the Sc<sub>2</sub>N surface and to elucidate the bonding characteristics between key atom pairs, namely C–O and Sc–O, we have performed a Crystal Orbital Hamilton Population (COHP) analysis using the LOBSTER code<sup>61–64</sup>, as shown in Figure 7a. The structural model identifying the specific C–O and Sc–O bonds under analysis is shown in Figure 7b. The two internal C–O bonds of the CO<sub>2</sub> molecule (C–O (1) and C–O (2)) exhibit strong bonding character, as indicated by the significant negative peaks in the pCOHP plots below the Fermi level. These states extend from approximately –10 eV up to –3 eV, and the corresponding integrated COHP (ICOHP) values are –10.65 eV and –10.68 eV, confirming their robust covalent nature. In contrast, the four Sc–O bonds that anchor the CO<sub>2</sub> molecule to the Sc<sub>2</sub>N surface show moderate bonding interactions, with ICOHP values ranging from –1.65 eV to –1.96 eV. The pCOHP curves for these bonds show modest bonding contributions below the Fermi level (–10 to –2 eV) and some antibonding states just above it (positive values), reflecting the partial covalent character of the Sc–O interactions. These antibonding features indicate back-donation from Sc d-orbitals to CO<sub>2</sub> anti-bonding orbitals, which contributes to CO<sub>2</sub> activation. Overall, the COHP analysis supports the conclusion that the Sc<sub>2</sub>N surface effectively activates CO<sub>2</sub> via moderate Sc–O interactions, while preserving the internal bonding structure of CO<sub>2</sub>.



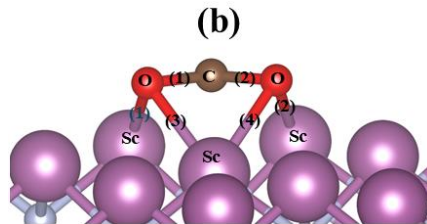
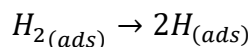


Figure 7. (a) Projected Crystal Orbital Hamilton Population (pCOHP) curves for the labeled atom pairs involved in the adsorption of a CO<sub>2</sub> molecule on the Sc<sub>2</sub>N surface. Curves are aligned to the Fermi level ( $E = 0$  eV). (b) Atomic structure and bond labeling for CO<sub>2</sub> adsorbed on the Sc<sub>2</sub>N monolayer. The numbered bonds correspond to those analyzed in the pCOHP plots shown in (a), with C–O bonds labeled as (1) and (2), and Sc–O bonds labeled as (1) to (4).

### 3.3. H<sub>2</sub> Dissociation

Efficient activation and dissociation of hydrogen molecules (H<sub>2</sub>) are a crucial step in catalytic hydrogenation, particularly in the CO<sub>2</sub> conversion reactions studied here. To assess the hydrogen activation capability of Sc<sub>2</sub>N MXene, we have investigated the dissociative adsorption of H<sub>2</sub>, shown in Figure 8.

The dissociation of H<sub>2</sub> on the Sc<sub>2</sub>N surface was modelled as a surface reaction from molecular adsorption to two adsorbed H atoms:



The corresponding dissociation energy was calculated as the total energy difference between these two adsorbed states:

$$E_{diss} = E_{2H/Sc_2N} - E_{H_2/Sc_2N}$$

Where  $E_{2H/Sc_2N}$  and  $E_{H_2/Sc_2N}$  are the total energies of the Sc<sub>2</sub>N surface with two individual hydrogen atoms and a molecular H<sub>2</sub> adsorbed on the surface, respectively.

Our results indicate that H<sub>2</sub> dissociation at the Sc<sub>2</sub>N surface is thermodynamically favorable, with a reaction energy of  $-1.71$  eV and an activation energy of  $0.75$  eV. While this represents a moderate energy barrier, it suggests that the reaction is kinetically feasible but would require energy input to proceed at a significant rate under ambient conditions. After dissociation, each hydrogen atom binds strongly to adjacent scandium sites, stabilised through the formation of Sc–H bonds. The high reactivity of Sc<sub>2</sub>N can be attributed to the metallic character of the surface and the presence of exposed Sc atoms, which promote electron transfer into the antibonding  $\sigma^*$  orbital of H<sub>2</sub>, thereby facilitating bond breaking. Such behaviour is consistent with trends reported for early transition

metal surfaces and MXenes, where low-coordinated metal sites lower the barrier for H<sub>2</sub> activation<sup>30</sup>.

Compared to previously studied MXenes and transition metal carbides/nitrides, where H<sub>2</sub> dissociation is moderately exothermic <sup>30</sup>, the dissociation energy on Sc<sub>2</sub>N (-1.71 eV) indicates a particularly strong interaction, highlighting the excellent ability of Sc<sub>2</sub>N towards H<sub>2</sub> activation.

The facile H<sub>2</sub> dissociation on Sc<sub>2</sub>N, combined with its strong CO<sub>2</sub> adsorption capacity (discussed in Section 3.2), positions Sc<sub>2</sub>N as a promising dual-activation platform, capable of simultaneously activating hydrogen and carbon dioxide, which is essential for efficient catalytic hydrogenation pathways toward methanol or methane.

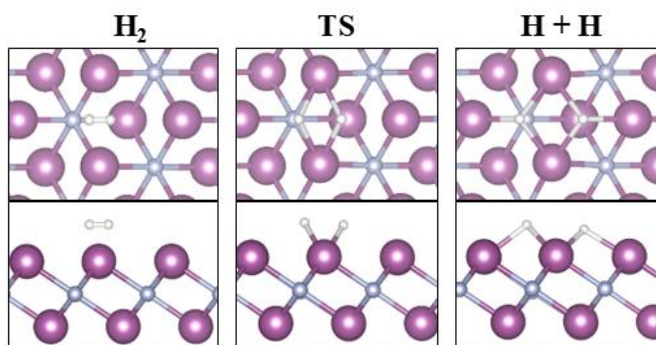


Figure 8. Top and side views of optimized geometries for H<sub>2</sub> molecular adsorption (left) and dissociative H adsorption (right) on the Sc<sub>2</sub>N surface. (Sc = purple, N = blue, H = white).

### 3.4. Adsorption Energies and Stabilities of Intermediates

The adsorption energies of key intermediates, including the CO<sub>2</sub>, COOH, HCOOH, HCO, H<sub>2</sub>CO, CH<sub>2</sub>OH, CH<sub>3</sub>OH, CH<sub>3</sub>, CH<sub>4</sub>, H<sub>2</sub> and H<sub>2</sub>O molecules and H atoms were found to be highly favourable, indicating strong binding with the Sc<sub>2</sub>N surface (see Table 1). This strong interaction is crucial to stabilize reaction intermediates during the CO<sub>2</sub> conversion process, which directly impacts the selectivity and efficiency of the catalyst. The optimal adsorbed geometries, characterized by the largest adsorption energies, are shown in Figure 9.

The large adsorption energies indicate that Sc<sub>2</sub>N offers a more stable platform for CO<sub>2</sub> reduction compared to other MXenes and traditional catalysts like Pt and Pd. For instance, the adsorption energy for HCOOH on Sc<sub>2</sub>N (-3.659 eV) is notably higher than that on Ti<sub>2</sub>N (-3.299 eV),

suggesting that Sc<sub>2</sub>N is more effective at stabilizing this intermediate, which is a crucial step in the methane production pathway<sup>65</sup>.

The stability of other intermediates at the Sc<sub>2</sub>N surface is comparable to observations for transition metal oxides. In other studies, it has been shown that metal oxide surfaces with appropriate terminations can stabilize reaction intermediates, leading to improved catalytic activity for CO<sub>2</sub> reduction<sup>66</sup>. The strong adsorption energies observed for intermediates like COOH and CH<sub>2</sub>OH on Sc<sub>2</sub>N suggest that this MXene may function similarly to modified metal oxides, providing enhanced stability in key reaction steps<sup>67</sup>.

Table 1. Adsorption geometries and energies of key intermediates on the Sc<sub>2</sub>N surface, compared with selected values from other catalysts. The adsorption energies of H and O atoms were calculated using  $\frac{1}{2}$  E(H<sub>2</sub>) and  $\frac{1}{2}$  E(O<sub>2</sub>) as reference states, respectively, to ensure consistency with standard DFT methodology<sup>30</sup>.

Intermediate	Site, Atom, Bond Length (Å)	E <sub>ads</sub> (eV) on Sc <sub>2</sub> N	E <sub>ads</sub> (eV) on Ti <sub>2</sub> N <sup>65</sup>	E <sub>ads</sub> (eV) on Pt(111) <sup>68, 69</sup>
CO <sub>2</sub>	hollow, oxygen, 2.420	-3.627	-3.13	-2.78
COOH	hollow, oxygen, 2.420	-5.184	-4.61	-4.32
HCOOH	hollow, oxygen, 2.420	-3.659	-3.299	-3.05
HCO	hollow, oxygen, 2.420	-5.728	-4.639	-5.94
H <sub>2</sub> CO	hollow, oxygen, 2.420	-4.067	—	—
CH <sub>2</sub> OH	hollow, oxygen, 2.420	-3.851	-3.18	-3.50
CH <sub>3</sub> OH	top, oxygen, 2.420	-2.673	—	—
CH <sub>3</sub>	hollow, carbon, 2.486	-3.562	-4.50	-4.00
CH <sub>4</sub>	hollow, carbon, Physical adsorption	-0.103	-2.93	-2.45
H <sub>2</sub> O	hollow, oxygen, 2.420	-1.127	—	—
H <sub>2</sub>	hollow, hydrogen, 2.135	-0.225	—	—
H	hollow, hydrogen, 2.076	-1.067	—	-2.71
O	hollow, hydrogen, 2.029	-5.744	—	-3.74



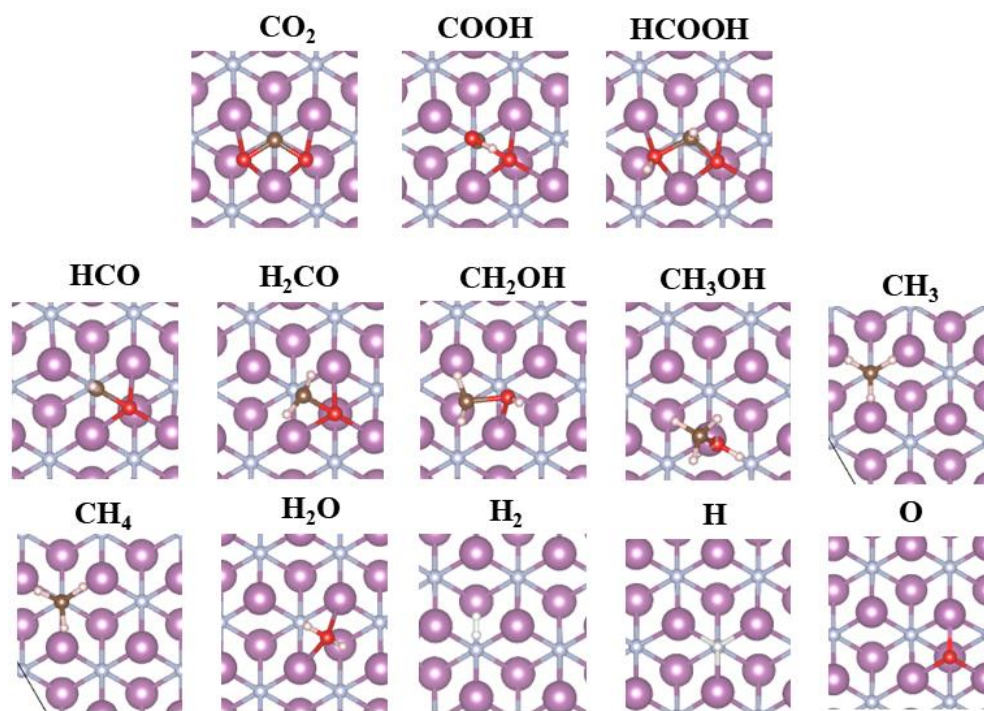


Figure 9. Top view of the lowest-energy adsorption structures of CO<sub>2</sub>, COOH, HCOOH, HCO, H<sub>2</sub>CO, CH<sub>2</sub>OH, CH<sub>3</sub>OH, CH<sub>3</sub>, CH<sub>4</sub>, H<sub>2</sub>O, and H<sub>2</sub> molecules and H and O atoms on the Sc<sub>2</sub>N surface (Sc = purple, N = blue, O = red, C = brown, H = white).

### 3.5. CO<sub>2</sub> hydrogenation pathway and activation energies

During CO<sub>2</sub> reduction, various carbon-based products can be generated, including carbon monoxide (CO), formic acid (HCOOH), formaldehyde (HCHO), methanol (CH<sub>3</sub>OH), ethylene (C<sub>2</sub>H<sub>4</sub>) and methane (CH<sub>4</sub>) [19]. In this study we were particularly interested in the pathway to methane through CO<sub>2</sub> hydrogenation, via a number of partially hydrogenated intermediates. Multiple mechanisms have been proposed for CH<sub>4</sub> production through CO<sub>2</sub> reduction. Here, we have focused exclusively on the CO<sub>2</sub> hydrogenation pathway that proceeds via the formation of formic acid (HCOOH). This pathway was selected based on previous theoretical studies indicating that the COOH → HCOOH conversion plays a central role in determining the efficiency of CO<sub>2</sub> reduction over transition metal and MXene surfaces<sup>21, 46, 47, 68</sup>. Accordingly, our investigation starts with the COOH intermediate and follows sequential hydrogenation steps through HCOOH, HCO, and beyond: CO<sub>2</sub> → COOH → HCOOH → HCO → H<sub>2</sub>CO → CH<sub>2</sub>OH → HOCH<sub>3</sub> → CH<sub>3</sub> → CH<sub>4</sub>, as shown in Figure 10. The adsorption energies of COOH and HCOOH on the Sc<sub>2</sub>N surface



were calculated to be -5.184 and -3.659 eV, indicating very strong interactions, which stabilizes the intermediates and facilitates further reduction.

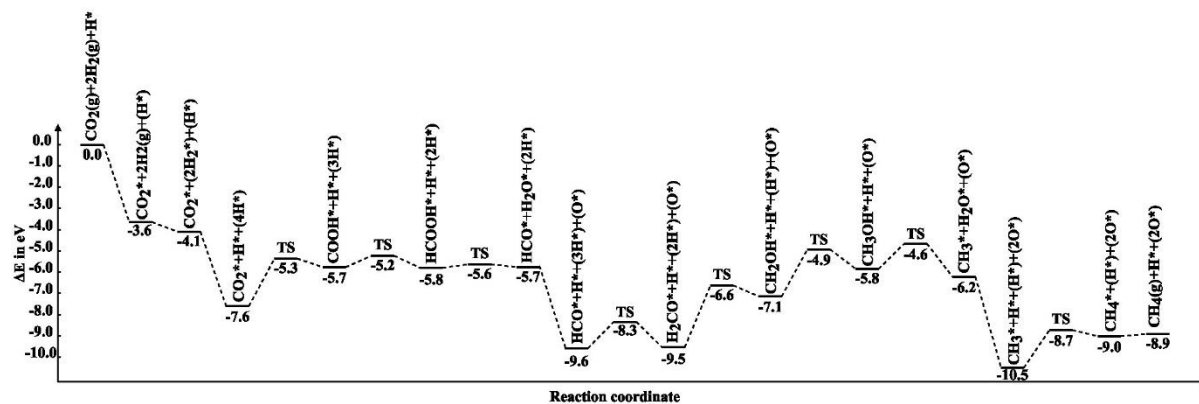


Figure 10. Reaction profile illustrating the hydrogenation of CO<sub>2</sub> and its intermediates to CH<sub>4</sub> on the Sc<sub>2</sub>N surface. Atoms in parentheses are included to maintain atomic balance.

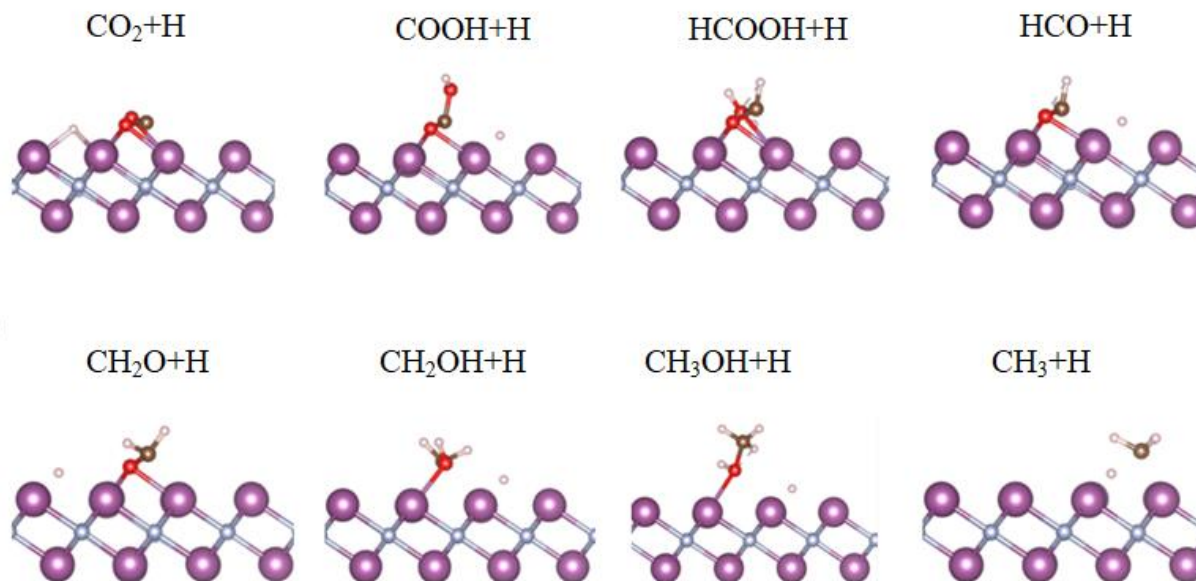


Figure 11. adsorption of a hydrogen atom next to the target molecules CO<sub>2</sub>, COOH, HCOOH, HCO, H<sub>2</sub>CO, CH<sub>2</sub>OH, CH<sub>3</sub>OH, and CH<sub>3</sub> (Sc = purple, N = blue, O = red, C = brown, H = white)



Figure 12. The selected reactions with their corresponding initial, transition (TS), and final states at the  $\text{Sc}_2\text{N}(001)$  surface (Sc = purple, N = blue, O = red, C = brown, H = white).

The  $\text{CO}_2$  reduction pathway selected for this study comprises eight steps, with each step involving the adsorption of a hydrogen atom next to the target molecule, i.e.  $\text{CO}_2$ ,  $\text{COOH}$ ,  $\text{HCOOH}$ ,  $\text{CHO}$ ,  $\text{H}_2\text{CO}$ ,  $\text{CH}_2\text{OH}$ ,  $\text{CH}_3\text{OH}$ , and  $\text{CH}_3$ , as illustrated in Figure 11. The reaction energies calculated via Equation (2) are presented in Table 2. To determine the rate-determining step characterized by the highest activation energy, we have employed Equation (3) to calculate the activation energy for

each reaction, listed in Table 2. Each elementary step in this pathway, shown in Figure 12, has been analyzed and compared with results from similar studies on MXenes and other catalytic surfaces, as described below.

**CO<sub>2</sub> + H → COOH:** The first reaction step, converting CO<sub>2</sub> to COOH, is highly endothermic (1.553 eV) and requires a considerable activation energy (2.222 eV), indicating that it is an energy-intensive initiation process. Previous studies have also suggested that activating CO<sub>2</sub> on MXene surfaces like Sc<sub>2</sub>N requires significant activation energies to be overcome, although these can be reduced with suitable surface functionalization<sup>31, 70</sup>. In comparison to Ti<sub>3</sub>C<sub>2</sub> and other MXenes, where activation energies for CO<sub>2</sub> to COOH conversion have been recorded at 1.8–2.0 eV, the process on Sc<sub>2</sub>N requires a little more energy, suggesting that this potential catalyst could benefit from structural modifications<sup>71, 72</sup>.

**COOH + H → HCOOH:** The second reaction step, reducing COOH to HCOOH, is exothermic with a reaction energy of -0.205 eV and a low activation energy of 0.550 eV, suggesting a more favorable energy profile. In other MXene studies, e.g. those involving Ti<sub>2</sub>C and Mo<sub>2</sub>TiC<sub>2</sub>, activation energies ranged between 0.4 and 0.6 eV for this step, i.e. very similar to Sc<sub>2</sub>N<sup>73, 74</sup>. This alignment highlights that Sc<sub>2</sub>N MXene could achieve similar catalytic performance to other MXenes, particularly in formic acid production, where low activation barriers are advantageous for efficient reduction.

**HCOOH + H → HCO + H<sub>2</sub>O:** The third step, converting HCOOH to HCO and H<sub>2</sub>O, has an almost zero reaction energy (0.010 eV) and an activation energy of only 0.152 eV, indicating that this step proceeds readily. Similar low-barrier pathways were observed in studies of metal oxide-supported MXenes, where the activation energies were comparably low. For instance, Mo<sub>2</sub>TiC<sub>2</sub> MXene on TiO<sub>2</sub> shows similarly low energy demands, supporting the suggestion that MXenes like Sc<sub>2</sub>N might efficiently facilitate this step in the reaction sequence<sup>73</sup>.

**HCO + H → H<sub>2</sub>CO:** Here, the step to form H<sub>2</sub>CO has a moderately positive reaction energy (0.290 eV) and an activation energy of 1.246 eV, i.e. a higher energy requirement than the two previous steps, but easier to achieve than the first hydrogenation step of the CO<sub>2</sub> molecule. Studies involving MXenes such as Ti<sub>3</sub>C<sub>2</sub> have shown slightly lower activation energies (around 1.0–1.1 eV) for this step, indicating again that Sc<sub>2</sub>N may benefit from additional surface optimization to match the efficiency of other MXenes in facilitating formaldehyde formation<sup>71, 72</sup>.

**H<sub>2</sub>CO + H → CH<sub>2</sub>OH:** The reduction of H<sub>2</sub>CO to CH<sub>2</sub>OH stands out as the most energy-intensive step, with a reaction energy of 2.619 eV and an activation energy of 2.916 eV, which may limit the overall efficiency of the reaction pathway over Sc<sub>2</sub>N. This high energy demand is consistent with reports on other MXenes like Nb<sub>2</sub>C, where energy requirements peak at this step, although alternative configurations on MXenes like V<sub>2</sub>C have shown potential to reduce the energy to around 2.5 eV<sup>46,57,75</sup>. Despite the challenges facing the application of Sc<sub>2</sub>N for this step, structural tuning or alloying could reduce the energy barrier and improve performance.

**CH<sub>2</sub>OH + H → CH<sub>3</sub>OH:** The conversion to methanol (CH<sub>3</sub>OH) is exothermic, with a reaction energy of -1.709 eV and an activation energy of 2.185 eV, indicative of a favourable methanol production pathway despite the high activation energy. Sc<sub>2</sub>N compares with Ti<sub>3</sub>C<sub>2</sub> and Mo<sub>2</sub>TiC<sub>2</sub>, where previous studies have identified similar activation energies in the range of 1.8–2.0 eV. This suggests that methanol production on Sc<sub>2</sub>N MXene could potentially be competitive with other MXenes under optimized conditions<sup>71,72</sup>.

**CH<sub>3</sub>OH + H → CH<sub>3</sub> + H<sub>2</sub>O:** This exothermic step with a reaction energy of -0.378 eV and activation energy of 1.192 eV indicates that forming CH<sub>3</sub> and H<sub>2</sub>O is feasible. The relatively low activation energy aligns well with findings on other MXenes like Ti<sub>3</sub>C<sub>2</sub>, where barriers are typically under 1.3 eV<sup>71,72</sup>. This similarity underscores that Sc<sub>2</sub>N could perform effectively at this stage, aligning with other promising MXenes.

**CH<sub>3</sub> + H → CH<sub>4</sub>:** The final step in methane production shows a positive reaction energy of 1.481 eV and an activation energy of 1.761 eV, comparable to MXenes like Nb<sub>2</sub>C and Ti<sub>3</sub>C<sub>2</sub>, which exhibit activation energies in the range of 1.5–1.8 eV for this step, Sc<sub>2</sub>N falls within the expected limits, suggesting it could be similarly viable for methane synthesis in a CO<sub>2</sub> reduction pathway<sup>46,71,72,75</sup>.

While the reaction energy profile (Figure 10) shows a strongly downhill thermodynamic trend, this behavior is largely influenced by the inclusion of co-adsorbed H and O species required to maintain stoichiometric balance between intermediates. This effect is due to their strong surface adsorption energies and is a standard feature in DFT-based reaction profiles that include co-adsorbed species.<sup>30</sup> These species bind very strongly to the Sc<sub>2</sub>N surface, leading to substantial energy drops at key points in the reaction coordinate. Notably, the adsorption energies of H and O (–1.067 and –5.744 eV, respectively) suggest that surface regeneration may be kinetically limited under reaction conditions. Such strong adsorption could hinder the release of products and block

active sites, ultimately affecting the catalytic turnover frequency. This issue has also been noted for other MXene systems, as discussed in the recent literature<sup>39</sup>, where excessive binding strength can impair the desorption of reaction intermediates such as OH\*, O\*, or H\*, leading to potential catalyst poisoning.

Table 2. Calculated reaction ( $E_{react}$ ) and activation ( $E_a$ ) energies for all hydrogenation elementary reactions on the Sc<sub>2</sub>N surface.

Reaction	$E_{react}$ (eV)	$E_a$ (eV)
$\text{CO}_2 + \text{H} \rightarrow \text{COOH}$	1.553	2.222
$\text{COOH} + \text{H} \rightarrow \text{HCOOH}$	-0.205	0.550
$\text{HCOOH} + \text{H} \rightarrow \text{HCO} + \text{H}_2\text{O}$	0.01	0.152
$\text{HCO} + \text{H} \rightarrow \text{H}_2\text{CO}$	0.29	1.246
$\text{H}_2\text{CO} + \text{H} \rightarrow \text{CH}_2\text{OH}$	2.619	2.916
$\text{CH}_2\text{OH} + \text{H} \rightarrow \text{CH}_3\text{OH}$	1.709	2.185
$\text{CH}_3\text{OH} + \text{H} \rightarrow \text{CH}_3 + \text{H}_2\text{O}$	-0.378	1.192
$\text{CH}_3 + \text{H} \rightarrow \text{CH}_4$	1.481	1.761

## 4. Conclusions

This study presents a comprehensive theoretical investigation of Sc<sub>2</sub>N MXenes as promising catalysts for CO<sub>2</sub> capture and conversion. Ab initio molecular dynamics simulations validate the thermal stability of Sc<sub>2</sub>N, indicating its viability under operational temperatures.

DFT simulations demonstrate that Sc<sub>2</sub>N has a high affinity for CO<sub>2</sub> with a large binding energy (–3.627 eV), exceeding the performance of comparable MXenes and traditional catalysts. The strong adsorption is facilitated by charge transfer from scandium d-orbitals, resulting in effective activation of the CO<sub>2</sub> molecule, as confirmed by charge density difference and COHP analyses.

The Sc<sub>2</sub>N surface also enables hydrogen dissociation and stabilizes key intermediates (e.g. COOH, HCOOH, CH<sub>2</sub>OH), supporting a viable hydrogenation pathway to CH<sub>4</sub>. Among the eight hydrogenation steps, CH<sub>2</sub>OH + H → CH<sub>3</sub>OH exhibits the highest activation energy (2.916 eV), marking it as the rate-determining step. Nevertheless, the overall pathway is thermodynamically downhill, suggesting favourable kinetics could be obtained under appropriate conditions.



Sc<sub>2</sub>N demonstrates strong potential for CO<sub>2</sub> capture and activation, with favourable adsorption energies and reaction energetics for intermediate hydrogenation steps along the HCOOH pathway. However, the highly exothermic energy profile of the reaction pathway is primarily driven by the strong adsorption of atomic H and O species. This trend suggests a risk of surface poisoning due to accumulation of these species at the surface, which could limit catalytic turnover under practical conditions. Therefore, while Sc<sub>2</sub>N is promising for CO<sub>2</sub> capture, its catalytic viability may depend on strategies to regenerate active sites, such as co-catalyst design, applied bias, or thermal treatment, to mitigate surface blocking and maintain continuous reactivity.

It is also important to note that all calculations were performed in the gas phase, neglecting solvent effects which could be present in an electrochemical environment. Solvent interactions may stabilize certain intermediates, modify adsorption energies, and lower activation barriers through solvation and hydrogen-bonding. The inclusion of solvent effects, either via implicit continuum models or explicit water layers, could thus provide deeper insight into the catalytic performance of Sc<sub>2</sub>N MXenes.

In summary, Sc<sub>2</sub>N MXenes combine strong CO<sub>2</sub> adsorption, intermediate stabilization, and electronic tunability, making them attractive candidates for CO<sub>2</sub> capture and methane production within carbon capture and utilisation (CCU) technologies. While the current study provides robust theoretical support, future work should incorporate solvent effects and explore regeneration mechanisms to enhance the practical applicability of Sc<sub>2</sub>N as a catalytic material.

## Acknowledgements

We are grateful to the Research Affairs Division of the Amirkabir University of Technology (AUT), Tehran, Iran, for financial support. SST thanks the UK Royal Society for an International Exchanges grant (IES\R3\223184).

This research has utilized the ARCHER2 UK National Supercomputing Service (<https://www.archer2.ac.uk>) through our membership of the HEC Materials Chemistry Consortium funded by UK Engineering and Physical Sciences Research Council (EP/R029431). The computational resources of the Advanced Research Computing at Cardiff (ARCCA) Division, Cardiff University, and HPC Wales were also employed for this study.

## Conflict of interest

The authors declare no conflict of interest.

## References

1. S. Muntone, *Education. com. The McGraw-Hill Companies. Retrieved*, 2013, **14**.
2. H. Ritchie and M. Roser, *Journal*, 2018.
3. K. O. Yoro and M. O. Daramola, in *Advances in carbon capture*, Elsevier, 2020, pp. 3-28.
4. I. P. O. C. Change, *Agenda*, 2007, **6**, 333.
5. H. Ritchie, P. Rosado and M. Roser, *Our world in data*, 2023.
6. J. Hansen, M. Sato and R. Ruedy, *Proceedings of the National Academy of Sciences*, 2012, **109**, E2415-E2423.
7. S. Solomon, G.-K. Plattner, R. Knutti and P. Friedlingstein, *Proceedings of the national academy of sciences*, 2009, **106**, 1704-1709.
8. R. K. Upadhyay, *American Journal of Climate Change*, 2020, **9**, 159.
9. C. Le Quéré, R. J. Andres, T. Boden, T. Conway, R. A. Houghton, J. I. House, G. Marland, G. P. Peters, G. R. van der Werf and A. Ahlström, *Earth System science data*, 2013, **5**, 165-185.
10. R. A. Houghton and A. A. Nassikas, *Global Biogeochemical Cycles*, 2017, **31**, 456-472.
11. I. C. Change, *Contribution of working group III to the fifth assessment report of the intergovernmental panel on climate change*, 2014, **1454**, 147.
12. I. Amer-Wahlin, C. Hellsten and H. Noren, *Obstet Gynecol*, 2002, **186**, 268-273.
13. E. S. Rubin, J. E. Davison and H. J. Herzog, *International Journal of Greenhouse gas control*, 2015, **40**, 378-400.
14. B. Metz, O. Davidson, P. Bosch, R. Dave and L. Meyer, *Contribution of Working Group II to the Fourth Assessment Report of the Intergovernmental Panel on Climate Change (IPCC)*, 2007.
15. M. Naguib, V. N. Mochalin, M. W. Barsoum and Y. Gogotsi, *Advanced materials*, 2014, **26**, 992-1005.
16. M. Naguib, M. Kurtoglu, V. Presser, J. Lu, J. Niu, M. Heon, L. Hultman, Y. Gogotsi and M. W. Barsoum, *Advanced materials*, 2011, **23**, 4248-4253.
17. B. Anasori, M. R. Lukatskaya and Y. Gogotsi, *Nature Reviews Materials*, 2017, **2**, 1-17.
18. B. Li, Y. Duan, D. Luebke and B. Morreale, *Applied Energy*, 2013, **102**, 1439-1447.
19. P. Wang, B. Wang and R. Wang, *Materials*, 2023, **16**, 6816.
20. U. U. Rahman, M. Humayun, U. Ghani, M. Usman, H. Ullah, A. Khan, N. M. El-Metwaly and A. Khan, *Molecules (Basel, Switzerland)*, 2022, **27**.
21. A. D. Handoko, K. H. Khoo, T. L. Tan, H. Jin and Z. W. Seh, *Journal of Materials Chemistry A*, 2018, **6**, 21885-21890.
22. L. Meng, L.-K. Yan, F. Viñes and F. Illas, *Journal of Materials Chemistry A*, 2024, **12**, 7856-7874.
23. R. Khanam, S. Fozia and M. A. Dar, *Sustainable Energy & Fuels*, 2024, **8**, 5595-5607.
24. M. Khazaei, M. Arai, T. Sasaki, C.-Y. Chung, N. S. Venkataramanan, M. Estili, Y. Sakka and Y. Kawazoe, *Advanced Functional Materials*, 2013, **23**, 2185-2192.
25. N. Goel, A. Kushwaha and M. Kumar, *RSC Adv*, 2022, **12**, 25172-25193.
26. M. Mozafari and M. Soroush, *Materials Advances*, 2021, **2**, 7277-7307.
27. S. Kumar and U. Schwingenschlögl, *Physical Review B*, 2016, **94**, 035405.
28. E. Balcı, Ü. Ö. Akkuş and S. Berber, *Journal of Physics: Condensed Matter*, 2018, **30**, 155501.
29. Q. Chen, D. Zhang, J. Pan and W. Fan, *Optik*, 2020, **219**, 165046.

532 30. M. López, Á. Morales-García, F. Viñes and F. Illas, *ACS Catalysis*, 2021, **11**, 12850-12857.

533 31. A. Jurado, K. Ibarra, Á. Morales-García, F. Viñes and F. Illas, *ChemPhysChem*, 2021, **22**, 2456-

534 2463.

535 32. P. Hohenberg and W. Kohn, *Physical Review*, 1964, **136**, B864-B871.

536 33. W. Kohn and L. J. Sham, *Physical Review*, 1965, **140**, A1133-A1138.

537 34. G. Kresse and J. Hafner, *Physical review B*, 1993, **47**, 558.

538 35. G. Kresse and J. Furthmüller, *Physical review B*, 1996, **54**, 11169.

539 36. G. Kresse and J. Hafner, *Physical Review B*, 1993, **48**, 13115.

540 37. J. P. Perdew, K. Burke and M. Ernzerhof, *Physical review letters*, 1996, **77**, 3865.

541 38. J. P. Perdew, K. Burke and M. Ernzerhof, *Physical Review Letters*, 1998, **80**, 891.

542 39. R. Morales-Salvador, J. D. Gouveia, Á. Morales-García, F. Viñes, J. R. B. Gomes and F. Illas, *ACS*

543 *Catalysis*, 2021, **11**, 11248-11255.

544 40. G. Kresse and D. Joubert, *Physical review b*, 1999, **59**, 1758.

545 41. J. Yu, L.-H. Xie, J.-R. Li, Y. Ma, J. M. Seminario and P. B. Balbuena, *Chemical Reviews*, 2017, **117**,

546 9674-9754.

547 42. I. B. Orhan, T. C. Le, R. Babarao and A. W. Thornton, *Communications Chemistry*, 2023, **6**, 214.

548 43. M. Faraji, A. Bafekry, M. M. Fadlallah, F. Molaei, N. N. Hieu, P. Qian, M. Ghergherehchi and D.

549 Gogova, *Physical Chemistry Chemical Physics*, 2021, **23**, 15319-15328.

550 44. H. J. Monkhorst and J. D. Pack, *Physical review B*, 1976, **13**, 5188.

551 45. S. Grimme, S. Ehrlich and L. Goerigk, *Journal of computational chemistry*, 2011, **32**, 1456-1465.

552 46. S. Sarabadani Tafreshi, M. Ranjbar, N. Taghizade, S. F. K. S. Panahi, M. Jamaati and N. H. de

553 Leeuw, *ChemPhysChem*, 2022, **23**, e202100781.

554 47. S. Sarabadani Tafreshi, S. F. K. S. Panahi, N. Taghizade, M. Jamaati, M. Ranjbar and N. H. de

555 Leeuw, *Catalysts*, 2022, **12**, 1275.

556 48. S. P. Thirumuruganandham, J. L. Cuevas Figueroa, A. T. Baños, D. J. Mowbray, T. Terencio and M.

557 O. Martinez, *ACS omega*, 2022, **8**, 2337-2343.

558 49. G. Mills, H. Jónsson and G. K. Schenter, *Surface Science*, 1995, **324**, 305-337.

559 50. H. Jónsson, G. Mills and K. W. Jacobsen, in *Classical and quantum dynamics in condensed phase*

560 *simulations*, World Scientific, 1998, pp. 385-404.

561 51. F. Hess, B. M. Smarsly and H. Over, *Acc Chem Res*, 2020, **53**, 380-389.

562 52. A. Bhat, S. Anwer, K. S. Bhat, M. I. H. Mohideen, K. Liao and A. Qurashi, *npj 2D Materials and*

563 *Applications*, 2021, **5**, 61.

564 53. Y. Wang, D. He, H. Chen and D. Wang, *Journal of Photochemistry and Photobiology C:*

565 *Photochemistry Reviews*, 2019, **40**, 117-149.

566 54. C. Kunkel, F. Viñes and F. Illas, *Energy & Environmental Science*, 2016, **9**, 141-144.

567 55. S. Matsuda, T. Mukai, S. Sakurada, N. Uchida and M. Umeda, *New Journal of Chemistry*, 2019,

568 **43**, 13717-13720.

569 56. X. Liu, L. Yao, S. Zhang, C. Huang and W. Yang, *Inorganic Chemistry*, 2024, **63**, 6305-6314.

570 57. B. Wang, A. Zhou, F. Liu, J. Cao, L. Wang and Q. Hu, *Journal of Advanced Ceramics*, 2018, **7**, 237-

571 245.

572 58. G. Henkelman, A. Arnaldsson and H. Jónsson, *Computational Materials Science*, 2006, **36**, 354-

573 360.

574 59. R. Khanam, A. Hassan, Z. Nazir and M. A. Dar, *Sustainable Energy & Fuels*, 2023, **7**, 5046-5056.

575 60. S. Fozia, A. Hassan, S. A. Reshi, P. Singh, G. A. Bhat, M. Dixit and M. A. Dar, *The Journal of*

576 *Physical Chemistry C*, 2023, **127**, 11911-11920.

577 61. R. Dronskowski and P. E. Bloechl, *The Journal of Physical Chemistry*, 1993, **97**, 8617-8624.

578 62. V. L. Deringer, A. L. Tchougréeff and R. Dronskowski, *The Journal of Physical Chemistry A*, 2011,

579 **115**, 5461-5466.



- 580 63. S. Maintz, V. L. Deringer, A. L. Tchougréeff and R. Dronskowski, *Journal of Computational*  
581 *Chemistry*, 2013, **34**, 2557-2567.
- 582 64. S. Maintz, V. L. Deringer, A. L. Tchougréeff and R. Dronskowski, *Journal of Computational*  
583 *Chemistry*, 2016, **37**, 1030-1035.
- 584 65. R. Morales-Salvador, Á. Morales-García, F. Vines and F. Illas, *Physical Chemistry Chemical*  
585 *Physics*, 2018, **20**, 17117-17124.
- 586 66. N. Atrak, E. Tayyebi and E. Skúlason, *Catalysis Science & Technology*, 2023, **13**, 3321-3336.
- 587 67. W. Gao, Y. Chen, B. Li, S. P. Liu, X. Liu and Q. Jiang, *Nat Commun*, 2020, **11**, 1196.
- 588 68. J. Scaranto and M. Mavrikakis, *Surface Science*, 2016, **648**, 201-211.
- 589 69. S. Gautier, S. N. Steinmann, C. Michel, P. Fleurat-Lessard and P. Sautet, *Physical Chemistry*  
590 *Chemical Physics*, 2015, **17**, 28921-28930.
- 591 70. B. M. Abraham, O. Piqué, M. A. Khan, F. Viñes, F. Illas and J. K. Singh, *ACS Appl Mater Interfaces*,  
592 2023, **15**, 30117-30126.
- 593 71. J. Li, Z. Wang, H. Chen, Q. Zhang, H. Hu, L. Liu, J. Ye and D. Wang, *Catalysis Science & Technology*,  
594 2021, **11**, 4953-4961.
- 595 72. T. Amrillah, A. R. Supandi, V. Puspasari, A. Hermawan and Z. W. Seh, *Transactions of Tianjin*  
596 *University*, 2022, **28**, 307-322.
- 597 73. T. Hou, Q. Luo, Q. Li, H. Zu, P. Cui, S. Chen, Y. Lin, J. Chen, X. Zheng, W. Zhu, S. Liang, J. Yang and  
598 L. Wang, *Nature Communications*, 2020, **11**, 4251.
- 599 74. L. Kabir, K. Wijaya and W.-C. Oh, *Sustainable Energy & Fuels*, 2024, **8**, 2535-2569.
- 600 75. S. Sarabadani Tafreshi, M. Ranjbar, M. Jamaati, S. F. K. S. Panahi, N. Taghizade, M. Torkashvand  
601 and N. H. de Leeuw, *Physical Chemistry Chemical Physics*, 2023, **25**, 2498-2509.

602